CONTROLLED GENERATION OF ARRAY BEAMS OF HIGHER ORDER ORBITAL ANGULAR MOMENTUM AND STUDY OF THEIR FREQUENCY DOUBLING CHARACTERISTICS

A thesis submitted towards partial fulfilment of
BS-MS Dual Degree Programme
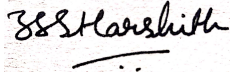
by

BACHIMANCHI SS HARSHITH

under the guidance of

DR. GOUTAM K. SAMANTA

PHOTONIC SCIENCES LABORATORY
PHYSICAL RESEARCH LABORATORY, AHMEDABAD

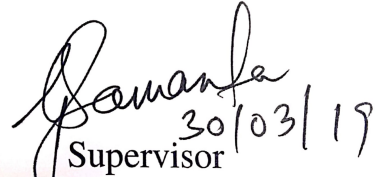INDIAN INSTITUTE OF SCIENCE EDUCATION AND RESEARCH PUNE

Certificate

This is to certify that this thesis entitled "*Controlled generation of array beams of higher order orbital angular momentum and study of their frequency doubling characteristics*" submitted towards the partial fulfilment of the BS-MS dual degree programme at the Indian Institute of Science Education and Research, Pune represents original research carried out by Bachimanchi SS Harshith at Physical Research Laboratory, Ahmedabad, under the supervision of Dr. Goutam K. Samanta during the academic year 2018-2019.
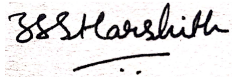
Student
BACHIMANCHI SS HARSHITH
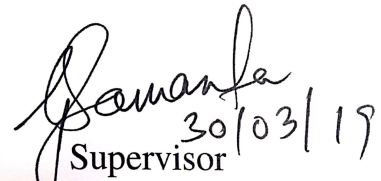
Supervisor
DR. GOUTAM K. SAMANTA

Declaration

I hereby declare that the matter embodied in the report entitled "*Controlled generation of Array beams of higher order orbital angular momentum and study of their frequency doubling characteristics*" are the results of the investigations carried out by me at the Division of Atomic, Molecular and Optical Physics, Physical Research Laboratory, Ahmedabad, under the supervision of Dr. Goutam K. Samanta and the same has not been submitted elsewhere for any other degree.

Student
BACHIMANCHI SS HARSHITH

Supervisor
DR. GOUTAM K. SAMANTA

Acknowledgements

Abstract

Optical vortices, beams carrying orbital angular momentum (OAM) per photon are of paramount interest in recent times for their wide variety of applications in particle trapping and micro-manipulation, material lithography and quantum information. Due to the presence of a helical phase variation in propagation and an undefined phase at the centre, these beams have a phase singularity in their wavefront, resulting in the doughnut-shaped intensity distribution. Though the vortex beams have been widely explored in the past, the recent advancements on mutli-channel quantum-communication systems, multiple-particle trapping, single-shot material ablation, demand an array of optical vortices in a simple experimental scheme.

The present work elaborates on a novel experimental scheme to generate high power, ultrafast, higher order optical vortex arrays. Simply by using a dielectric microlens array (MLA) and a plano-convex lens we have generated array beams carrying the spatial property of the input beam. Considering the MLA as a 2D sinusoidal phase grating, we have numerically calculated the intensity pattern of the array beams in close agreement with the experimental results. We have also theoretically derived the parameters controlling the intensity pattern, size and the pitch of array and verified experimentally. The single-pass frequency doubling of the vortex array at 1064 nm in a 1.2 mm BiBO crystal produced green vortex arrays of orders as high as $l_{sh} = 12$, twice the order of the pump array beam, with a conversion efficiency as high as $\sim 3.65\%$.

Additionally, the near field diffraction effects of MLA, have been studied in this work, indicating the self-imaging effect at Talbot planes. Using the MLA as an array illuminator at 1064 nm on to a 1.2 mm BiBO crystal, we have experimentally verified the second harmonic Talbot effect at 532 nm. In order to overcome the stringent dependence of the MLA parameters on the Talbot planes, we have devised a generic experimental scheme based on Fourier transformation technique, to independently tune the Talbot lengths.

List of Publications

Journal Publications

1. *Controlled generation of Array beams of higher order orbital angular momentum and study of their frequency doubling characteristics*,

   B. S. Harshith and G. K. Samanta,

   arXiv, 1903.00164 (2019). [*Manuscript under review at nature: Scientific Reports*]

Conference papers:

1. *Linear and non-linear generation of high power, ultrafast optical vortex arrays using a microlens array*,

   B. S. Harshith and G. K. Samanta,

   International Conference on Fiber Optics and Photonics, IIT Delhi. Paper No. TP164, Proceedings of the Photonics-2018, ISBN-978-93-88653-41-1 (2018).

2. *Generation and Frequency-conversion of Optical Vortex Arrays with Controlled Intensity Distribution*,

   B. S. Harshith and G. K. Samanta,

   CLEO, San Jose, California, USA: Science and Innovations, JW2A.68. Optical Society of America (2019).

Contents

List of Figures

4

Chapter 1

Introduction

This chapter is divided into several sub-sections to give a brief introduction on topics which are conceptually related to the work presented in this thesis. The first section gives a brief introduction on structured optical beams and discusses various ways to generate beams carrying orbital angular momentum (OAM). Subsequent sections give a brief idea on second-order non-linear processes and the non-linear interaction of structured optical beams.

1.1   Structured optical beams

Fundamentally, a laser beam having a transverse Gaussian spatial profile is characterized by three important properties. The transverse phase, polarization and the amplitude. In order to overcome certain limitations in laser beam optics and also to extend their applications in new fields of science and technology, efforts have been made to develop deeper understanding of the spatial properties of the beam, by modulating the beam characteristics using different spatial modulators. This resulted in the generation of a new class of beams known as the structured optical beams.

Bessel-Gaussian beams, Airy beams and Laguerre-Gaussian beams are few of such beams, which fall under the class of structured beams. Structured beams not only preserve the properties of input laser beams, but also carry additional properties such as OAM, self-healing,

non-diffraction, etc. Different spatial modulators are now commercially available for the generation of different structured beams starting from axicons for the generation of Bessel beams, spiral phase plates for the generation of optical vortices and nematic liquid crystal displays for dynamically modulating any phase profile. In the present study, we concentrate on one such class of structured beams, carrying orbital angular momentum per photon, known as the optical vortex beams.

1.1.1 Optical Vortices

Optical vortices, structured beams with helical wavefront carrying OAM per photon are generated by spatial mode conversion of Gaussian beams. A laser beam with a transverse spatial Gaussian profile on reflection / transmission through spatial mode converters such as spiral phase plates (SPPs) [1], q-plates [2], liquid crystal based spatial light modulators (SLMs) [3], pick up a helical phase factor, exp($il\varphi$), where φ is the azimuthal angle and l is the topological charge or OAM order of a vortex beam. Due to the presence of a helical phase variation in propagation and an undefined phase at the center, the vortex beams have a phase singularity in its wavefront, resulting in the doughnut-shaped intensity distribution.

1.1.2 Generation of Optical Vortics

The simplest method to generate an optical vortex is to pass it through an optical element known as Spiral phase plate (SPPs). As suggested in Fig.1.1, the architecture of a spiral phase plate [4], it can be noticed that the optical element is of constant thickness in the radial direction, but with a step wise increase in the thickness along the azimuthal direction. let's consider the difference in thickness between the thickest and the thinnest portions is h. Then, the thickness of the SPP, as a function of the azimuthal plane can be written as,

$$t(\varphi) = \frac{h\varphi}{2\pi},$$
(1.1)

where φ is the azimuthal angle, ranging from 0 to 2π. Considering the plate to be in a background of refractive index, n_0, with the refractive index of the plate being, n, and the vacuum wavelength of the input radiation being λ, the total optical path length $O(\varphi)$ (the product of physical length and refractive index) of the SPP, can be written as [4],

$$O(\varphi) = \left(h - \frac{h\varphi}{2\pi} \right) n_0 + \frac{h\varphi}{2\pi} n, \tag{1.2}$$

Neglecting the constant term arising from the background refractive index, the phase contrast, $\psi(\varphi)$, produced by the SPP can be obtained by multiplying a constant factor of $\frac{2\pi}{\lambda}$ to the optical path length, $O(\varphi)$ (Eq. (1.2)) as,

$$\psi(\varphi) = \frac{h\varphi}{\lambda}\left(n - n_0 \right). \tag{1.3}$$

If the thickness, h, of the SPP is designed in such a way that,

$$\frac{h}{\lambda}\left(n - n_0 \right) = l, \tag{1.4}$$

the output field, E_{out}, from the SPP, can be obtained as,

$$E_{out} = e^{il\varphi} E_{in}, \tag{1.5}$$

where, E_{in}, is the input field to the SPP. Notice that, here l is the topological charge of the optical vortex generated. When a plane wave traverses the SPP, the rays get delayed, depending on their position in the azimuthal plane. The rays traversing steps of larger height will get delayed longer as compared to the rays traversing shorter steps. As a cumulative effect, a helical wavefront is generated from a plane wavefront (Eq. 1.5). Depending on the required topological charge, l, and input wavelength, λ, the step heights and lateral widths of the steps in the SPPs are designed, as to accumulate the new scaled helical phase over the same azimuthal angles (Eq. 1.4 and 1.5).

Fig. 1.1 (b), pictorially represents the generation of an optical vortex beam of OAM order, $l=1$, from an input plane Gaussian profile. As discussed before, due to a helical phase variation in propagation and an undefined phase at the center, the vortex beams posses a doughnut shaped intensity distribution.

(a) Spiral Phase Plate (SPP)

(b) SPP ($l = 1$)
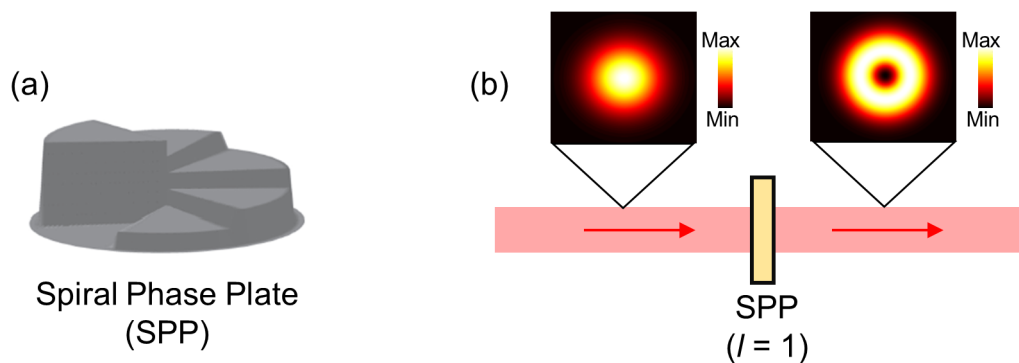
Figure 1.1: (a) Stair case spiral phase plate (SPP) and (b) Vortex beam generation with SPP

Mathematically, the transverse electric field amplitude distribution of a vortex beam can be represented by Eq. 1.6 [5],

$$E_l \sim \left[\frac{(r\sqrt{2})^l}{(w_g)^l} \, exp\left(\frac{-r^2}{w_g{}^2}\right) exp(il\varphi) \right] \tag{1.6}$$

As it can be seen, the equation still preserves the Gaussian beam characteristics (central term), along with additional properties. The last term in the equation represents the helical phase factor embedded to the Gaussian beam, while passing through spatial mode converters such as SPP. The first term is responsible for the size of the central dark core. As suggested from the expression (Eq. 1.6), the size of the dark core increases with the OAM order, l, of the vortex beam. Here w_g is the beam waist of the Gaussian confined vortex beam and r is the radial distance of the beam in the azimuthal plane. The intensity distribution (Fig. 1.1 (b)) of a vortex beam can be obtained by taking the conjugate product of the equation, Eq. 1.6. As a result, the helical phase cancels out and does not contribute, to the spatial intensity profile.

This result, indicates the fact that, the OAM order and its sign, cannot be detected directly from the intensity distributions alone. Hence we need specialized methods to detect the phase to characterize the order.

1.1.3 Detection of Optical Vortices

As noted in the previous section, an optical vortex, fundamentally being a phase structure, cannot be detected by the intensity profiles alone. As a natural tool for phase studies, interferometric techniques have been tried out and found successful in the detection of optical vortices. It is found that, the interference between a tilted plane Gaussian wave and an optical vortex will generate fork like interferograms. By counting the number of additional bright lines in the pattern and the direction of the fork, the order of the beam can be estimated. Similarly, a vortex beam when combined with its mirror image along the same axis, generates a petal like lobe structure [4]. Though the vortex charge can be known by counting the number of lobes in the petal structure ($2l$ number of lobes), However, the sign of the vortex charge cannot be estimated by this technique. Though both these methods, are rich in rigour and proved successful in detecting the vortex charge, a simpler variant of the above methods, using a tilted lens is found widely useful in detecting maximum OAM order in a vortex beam [6].

A vortex beam propagating through a tilted lens, gets split into its characteristic lobes. It is understood from the previous sections that, a vortex beam of order, l, carries a helical phase of '$2\pi l$' along the azimuthal plane, in one complete rotation '2π'. On the other hand, a convex lens tilted in radial direction, will introduce an astigmatic effect along the focal plane, thus bringing the diametrically opposite points on one of the axis (horizontal axis) closer than the other points (vertical axis). This leads to an interference in one axis, forming characteristic lobes. As an example, Fig. 1.2, depicts the detection of an $l = 2$ optical vortex by tilted lens technique. As suggested in Fig. 1.2, a total phase of '4π' is present along the azimuthal plane, for an $l = 2$ vortex. When propagated through a tilted lens, the diametrically opposite points, corresponding to phase positions, 3π and π, converge towards the center, forming a bright lobe,

due to constructive interference ('2π' phase difference). The vertical points continue to stay in their respective positions, as the tilt is introduced only in the radial direction. As a combined effect, the top and bottom points corresponding to phase positions 0 or 4π and 2π, together with the central bright lobe, form a three lobe structure, as shown in Fig. 1.2. Similarly, an higher order optical vortex of charge l, splits into $n = l + 1$ lobes, while passing through a tilted lens. The lobe structure can be observed along the depth of the focus of the tilted lens. The slight tilt in the lobe structure is due to the helical phase variation in propagation and the position of imaging. Consequently, the lobe structure, flips its direction for an oppositely charged vortex.
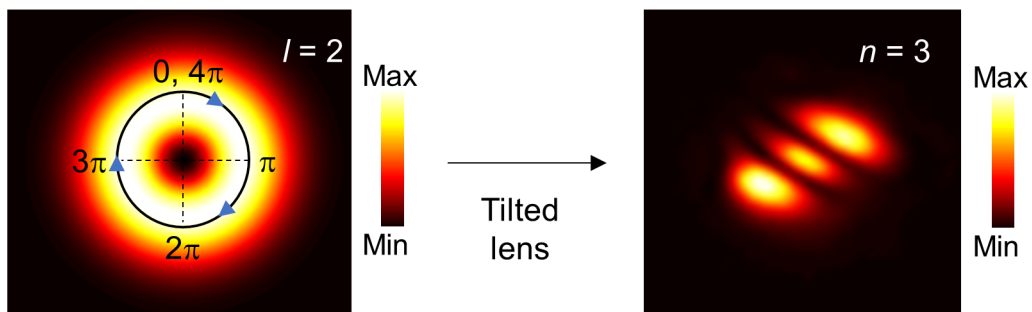
Figure 1.2: Detection of vortex order for an $l = 2$ vortex beam through tilted lens technique

Over the years, the vortex beams are found useful in a wide variety of applications in science and technology including particle trapping, micro-manipulation [7] and material lithography [8]. Also, as the vortex beams can posses a infinite degrees of freedom in OAM, they are utilized for OAM multiplexing and quantum information [9, 10]. Because of their unique properties, the vortex beams have found a great deal of attention in the non-linear optics as well, with some interesting results observed over recent years. The upcoming section introduces the basics of second order non-liner processes and the behaviour of vortex beams in non-linear regimes.

1.2   Non-linear Optics

An electric field when passed through a dielectric medium induces dipole moment per unit volume or simply, the polarization. The induced polarization, **P**, by the applied electric field can be written as a power series, as,

$$\mathbf{P} = \varepsilon_0 \, \chi^1 \, \mathbf{E} + \varepsilon_0 \, \chi^2 \, \mathbf{E}^2 + \varepsilon_0 \, \chi^3 \, \mathbf{E}^3 + ... \tag{1.7}$$

Here, χ^n, is the nth order susceptibility tensor, ε_0 is the permittivity of the free space and **E** is the input electric field. As can noted from the Eq. 1.7, the higher order polarization effects are proportional to the nth power of the susceptibility, signifying that high power light sources are required to achieve higher order polarization effects, considering the low χ^n values. In general all the naturally observable optical phenomenon such as the dispersion, reflection, refraction, etc are first order effects, where a feeble electric field is sufficient for polarizing materials. Hence the polarization is linearly proportional to the electric field (first term, Eq. 1.7). When, the light is intense enough to generate second order dipole moments, a new field, nonlinear optics is often discussed. Typically, the second order non-linear effects result in the generation of new frequencies, with the help of high power laser sources. Few of the non-linear frequency generation processes, which arise as a consequence of χ^2 non-linearities are second harmonic generation (SHG), sum-frequency generation (SFG), difference-frequency generation (DFG), etc. For the best interest of the work done in this thesis, the brief discussion presented in the following section will be limited to second harmonic generation (SHG).

1.2.1   Second-Harmonic Generation

In second harmonic generation (SHG) process, two photons of same input frequency ($\omega_1 = \omega_2 = \omega$), are added, to generate a new photon of twice the energy of the input photon ($\omega_3 = 2\omega$)

(or at half the wavelength). In order to achieve this, the interacting waves in the non-linear media should obey the relations corresponding to energy conservation ($\hbar = 1$) and momentum conservation, as follows,

$$\omega_3 = \omega_1 + \omega_2 = 2\omega \tag{1.8}$$

$$k_{2\omega} = 2k_\omega. \tag{1.9}$$

The interaction is most efficient, when both the relations (Eq. (1.8) and (1.9)) are satisfied. In order to achieve phase matching in non-linear crystals, two important techniques have been developed, birefringent phase matching (BPM) and quasi-phase matching (QPM). For the present discussion, the brief description on phase matching will be limited to birefringent phase matching. However, discussions on quasi-phase matching can be found in the following reference [11].

1.2.1.1 Birefringent phase matching

The phenomena of polarization dependent refractive index is known as the birefringence. By exploiting the birefringence of a non-linear crystal, phase matching between the interacting waves can be achieved. Typically, birefringent crystals will have an optic axes, along which the transmitted light suffers no birefringence. The basic principle behind the BPM is that, by choosing a proper propagation direction inside the crystal, the phase velocities of interacting waves can be adjusted, so that the wave-vectors satisfy the phase matching conditions. Based on input wave and output wave polarizations, the birefringent-phase matching can be divided into two types, type-I and type-II.

1. Type-I phase matching: The polarization of input electric fields is orthogonal to the generated field. ($e + e \rightarrow o$ and $o + o \rightarrow e$). Here, e and o are symbolic representations of ordinary and extra-ordinary rays inside a birefringent crystal respectively.

12

2. Type-II phase matching: The polarization of input electric fields are orthogonal to each other. ($e + o \rightarrow e$).

Efforts have been made to understand the frequency doubling characteristics of Gaussian beams with birefringent crystals of various lengths [12, 13]. Recently, the frequency doubling characteristics of ultrafast vortex beams have been studied [14], revealing some interesting properties. As discussed in previous sections, optical vortices carry a helical of *exp(ilφ)* and OAM per photon. In the second harmonic generation process, two such photon carrying helical phase are added, to generate a helical phase twice that of the pump.

$$e^{il\varphi} + e^{il\varphi} \rightarrow e^{i(2l)\varphi} \tag{1.10}$$

That is, the SHG vortex beams will have the OAM order, twice that of the pump orders. This peculiar observation revealed a new property of OAM conservation in the SHG process.

With an increasing interest in the study of optical vortices and the recent advancements on multiple particle trapping [15], fast micro-machining [16] and multiplexing in quantum information [9], demand an array of optical vortices in a simple experimental scheme. In Chapter 2, we show a novel experimental scheme to generate an array of vortices, with the OAM order same as that of the pump beam, using a microlens array. Also, we have studied the frequency doubling characteristics of the array beams. In Chapter 3, we report on the near field diffraction effects of the microlens array and the second harmonic Talbot effect with controllable Talbot lengths.

Chapter 2

Generation of Array Beams carrying OAM

This chapter constitutes the following manuscript.

1. *Controlled generation of Array beams of higher order orbital angular momentum and study of their frequency doubling characteristics*,

   B. S. Harshith and G. K. Samanta

   arXiv, 1903.00164 (2019). [*manuscript under review at nature: Scientific Reports*]

The present chapter elaborates on a novel experimental method to generate an array of optical beams of any input spatial profile. As a proof of principle, we generate an array of vortex beams, each carrying the OAM, same as that of the input beam, at all the positions in the array.

2.1   Introduction

As discussed in the previous chapters, optical vortices, doughnut shaped optical beams with helical wavefront, carry orbital angular momentum (OAM) per photon. Typically, the optical vortices are generated by impinging a helical phase factor $exp(il\varphi)$ (where, φ is the azimuthal

angle and l is the topological charge or the order of a vortex beam), to the Gaussian beams with the help of spatial mode converters including spiral phase plates (SPPs) [1], q-plates [2], and holographic spatial light modulators (SLMs) [3]. Since their discovery, the vortex beams have found a great deal of attention for their wide range of applications in a variety of fields in science and technology including particle trapping and micro-manipulation [7], quantum information [10] and micromachining [8]. However, the recent advancements on multiple particle trapping and tweezing [15], fast micromachining [16], and multiplexing in quantum information [9] demand optical beams with vortex arrays in a simple experimental scheme. While majority of the existing mode converters transform the Gaussian beam into a single vortex beam, the intrinsic advantage of the dynamic phase modulation through holographic technique allow the SLMs to generate vortex arrays directly from a Gaussian beam [17]. However, the low damage threshold of SLMs restrict their usage for high power vortex array applications. As such one need to explore alternative techniques to generate array of vortex beams.

Efforts have been made to generate optical beamlet arrays using annular apertures with optical coherence lattices [18] and modified Fresnel zone plates [19]. In addition to the difficulty of manufacturing such devices, the power loss in such devices restrict their use for high power operations. On the other hand, plasmonic metasurface nano apertures [20] and amplitude gratings [21] have produced optical vortex arrays in Talbot planes through self-imaging. Unfortunately, the stringent dependence of the input grating parameters on the self-imaging, results in limited or no control on the properties of the vortex array. Here, we report a simple experimental scheme based on a dielectric microlens array (MLA) and a plano-convex lens to generate high power array beams carrying the spatial property of the input beam. Using ultrafast, high power vortex beams of orders as high as, $l = 6$, at 1064 nm in the input, we have generated vortex beam arrays and subsequently frequency-doubled into vortex arrays at a new wavelength. Using simple mathematical treatment, we have numerically calculated the intensity distribution of the vortex array and also derived the parameters controlling the vortex array in close agreement with the experimental results.

15

2.2 Experimental Setup

The schematic of the experimental setup is shown in Fig. 2.1. A 5 W Yb-fiber laser with spectral linewidth of 15 nm centred at 1064 nm providing femtosecond pulses of width ~ 260 fs at a repetition rate of 78 MHz is used as the pump laser source. The input power and polarization to the setup is varied using a half waveplate ($\lambda/2$) and polarizing beam splitter cube (PBS1). A PBS splits the input beam based on the polarization content of the Beam. The reflective port of the PBS allows the vertical polarization, $|V\rangle$, and the transmissive port allows the horizontal polarization, $|H\rangle$. The weights of the polarizations, $a|H\rangle + b|V\rangle$, is controlled by the angle of the fast-axis of the half-wave plate to the input beam polarization. The fast-axis of a birefringent material, is axis along with there is no change in the refractive index. Hence by controlling the input polarization angle to the fast axis, a particular input polarization state can be arbitrarily projected in to a superposition state. The $|H\rangle$ polarized beam is expanded and collimated using a telescopic combination of lenses, L1 and L2 of focal length, $f = 50$ mm and $f = 100$ mm, respectively.

Using two spiral phase plates, SPP1 and SPP2, with phase winding corresponding to vortex orders $l = 1$ and $l = 2$, respectively and the vortex doubler [14] comprised with the PBS2, quarter-wave plate ($\lambda/4$) and mirror, M1, we have converted the Gaussian beam into vortex of order, $l = 1-6$. The working principle of vortex doubler scheme can be understood as follows. The $|H\rangle$ polarized beam transmitted through the PBS2, will acquire a vortex charge of $l = 1$ (let's say),while propagating through the SPP1. The quarter-wave plate ($\lambda/4$) at +45° (fast-axis angle), converts the $|H\rangle$ polarized beam into a left-circularly polarized beam, $|L\rangle$. On reflection from the plane mirror M1, $|L\rangle$ polarized beam will get flipped to a right-circularly polarized beam $|R\rangle$. On the other hand, the vortex charge, l, will change its sign from $l = 1$ to $l = -1$ on reflection from the mirror M1. So, in the return pass, we have an $|R\rangle$ polarized vortex beam of order, $l = -1$. Now, the $|R\rangle$ polarized beam gets converted to a $|V\rangle$ polarized beam, after traversing the quarter-wave plate ($\lambda/4$) in the return pass. Also, now the beam sees
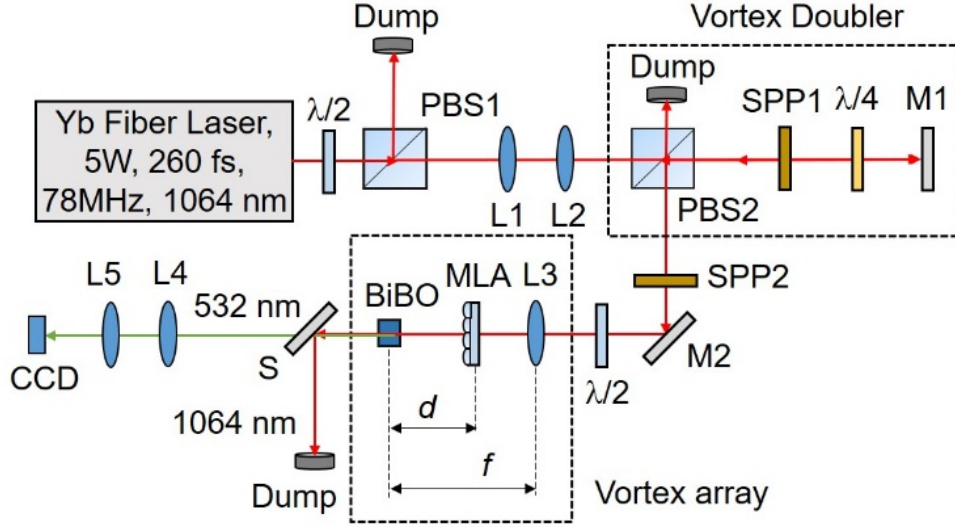
Figure 2.1: Schematic of the experimental setup to generate vortex beam array. $\lambda/2$, half-wave plate; PBS1-2, polarizing beam splitter cube; SPP1-2, spiral phase plates; $\lambda/4$, quarter-wave plate; L1-5, lenses; M1-2, mirrors; BiBO, nonlinear crystal for frequency doubling; MLA, microlens array; S, wavelength separator; CCD, CCD camera.

the direction of phase variation of the SPP1, in the opposite direction to that of the forward pass. As a result, the beam acquires an additional phase of order $l = -1$ to the existing $l = -1$ charge, making it a $|V\rangle$ polarized vortex beam of order $l = -2$. As discussed before, the PBS2 will now reflect the $|V\rangle$ polarized beam. Essentially, using a single SPP (SPP1), we have doubled the vortex charge. Using different combinations of SPP1 and SPP2 of orders $l = 1$ and $l = 2$, we can generate optical vortices of orders, $l_p = 1, 2, 3, 4, 5$ and 6.

The pump vortex beam of order, l_p, on propagation through the lens L3 of focal length $f = 300$ mm, and the microlens array (MLA) (Thorlabs MLA 300-14AR) consisting with 391 lenslets of focal length, $f_{MLA} = 18.6$ mm resembling a 2D sinusoidal phase pattern, is Fourier transformed to produce vortex array at the back focal plane of the lens L3 [22]. The distance, d, of the MLA from the back focal plane of L3 modulates the pitch of the vortex array and the focal length, f of the lens L3 determines the diameter of individual vortices in the array. A 1.2 mm long and 4 x 8 mm^2 in aperture bismuth borate (BiBO) crystal [23], cut for type-I (e + e $\rightarrow$

o) frequency doubling in optical yz-plane ($\phi = 90°$) with internal angle of $\theta = 168.5°$ at normal incidence, is placed at the Fourier plane for second harmonic generation (SHG) of vortex arrays at 1064 nm into green at 532 nm. The frequency doubled vortex array is extracted from the undepleted pump using a wavelength separator, S, and imaged at the CCD camera plane using lenses, L4 and L5.

Section 2.3, discusses the theory behind the generation of array beams of any input spatial profile, using a microlens array and a convex lens. As a proof of principle, we generate an array of optical vortices and draw a comparison between the theoretical and experimental results. Later the frequency doubling of the arrays in the non-linear BiBO crystal is presented.

2.3   Theory

To understand the formation of arrays in the present experimental scheme (Fig. 2.1), we have approximated the MLA as a 2D sinusoidal phase grating [24] of pitch, Λ, and sinusoid amplitude thickness, s [25]. The transverse field amplitude distribution of any input electric field, E_{in}, after the microlens array can be written as [22]

$$E_{MLA} \sim t_A(x,y)\, E_{in} \tag{2.1}$$

where,

$$t_A(x,y) = exp\left[i\,\frac{m}{2}\,sin\left(\frac{2\pi x}{\Lambda}\right)\right] exp\left[i\,\frac{m}{2}\,sin\left(\frac{2\pi y}{\Lambda}\right)\right] \tag{2.2}$$

is the amplitude transfer function of the microlens array. Here $m = 2\pi(n-1)s/\lambda$ is the phase contrast of the grating [25] with λ being the wavelength of the input radiation. Eq. 2.2, can

represented in terms of nth order Bessel functions of first kind, using the Jacobi-Anger identity,

$$exp(iz\sin\theta) \equiv \sum_{n=-\infty}^{\infty} J_n(z)\,exp(in\theta), \tag{2.3}$$

as,

$$t_A(x,y) = \sum_{p=-\infty}^{\infty} J_p\left(\frac{m}{2}\right) exp\left(i\frac{2\pi px}{\Lambda}\right) \sum_{q=-\infty}^{\infty} J_q\left(\frac{m}{2}\right) exp\left(i\frac{2\pi py}{\Lambda}\right) \tag{2.4}$$

where J_p and J_q are the Bessel functions of first kind of orders p and q. The Fraunhofer (far-field) diffraction pattern of the microlens array can be obtained by taking the Fourier transform of Eq. 2.1. Experimentally, this can be done by using the convex lens as a Fourier transforming element (Fig. 2.1).

According to Fourier transformation theory [22], any object can be Fourier transformed by placing the object after the lens at an arbitrary distance, d, from the focal plane [26]. The basic principle of the technique is pictorially represented in Fig. 2.1 (inset: vortex array), where the object (MLA) placed at a distance $(f-d)$ after the lens of focal length f, is Fourier transformed into array beams at the back focal plane for input beam of any spatial profile. Therefore, the field amplitude distribution of array beams can be obtained by taking the Fourier transform of Eq. 2.1, as,

$$E \sim \sum_{p,q=-\infty}^{\infty} J_{p,q}(m)\,\delta_{x,y}(d,\lambda) \otimes \mathfrak{F}(E_{in}) \tag{2.5}$$

where,

$$\delta_{x,y}(d,\lambda) = \delta\left(\frac{1}{f\lambda}\left[x-p\left(\frac{\lambda d}{\Lambda}\right)\right], \left(\frac{1}{f\lambda}\left[y-p\left(\frac{\lambda d}{\Lambda}\right)\right]\right), \tag{2.6}$$

19

$$J_{p,q}(m) = J_p\left(\frac{m}{2}\right) J_q\left(\frac{m}{2}\right). \tag{2.7}$$

Here $\mathfrak{F}(E_{in})$, is the Fourier transform of input electric field E_{in} . As suggested in Eq. 2.5, the convolution of $\mathfrak{F}(E_{in})$, with the 2D delta function, $\delta_{x,y}(d,\lambda)$, as represented in Eq. 2.6, replicates $\mathfrak{F}(E_{in})$ at positions determined by individual delta peaks, as a function of the input wavelength, λ, and distance, d. Therefore, one can generate array beams of desired intensity distribution by using suitable spatial profile of the input field.

Considering the input field to the MLA, E_{in}, to be a Gaussian confined vortex beam of order l,

$$E_{in} \equiv E_l \sim \left[\frac{(r\sqrt{2})^l}{(w_g)^l} exp\left(\frac{-r^2}{w_g{}^2}\right) exp(il\varphi) \right] \tag{2.8}$$

the Fourier transform of the beam can be obtained as,

$$\mathfrak{F}(E_l) \sim \left[\frac{(r\sqrt{2})^l}{(w_0)^l} exp\left(\frac{-r^2}{w_0{}^2}\right) exp(il\varphi) \right] \tag{2.9}$$

It can be noticed that, the Fourier transform of an optical vortex is the same function, similar to the property of a Gaussian function. However, the input beam width, w_g, has been to focussed into a Gaussian embedded vortex beam waist of, $w_0 = f\lambda/\pi w_g$. Given that, $\mathfrak{F}(E_l)$ (Eq. 2.9), is also an optical vortex of order l, we expect an array of vortices at the focal plane, as suggested by Eq. 2.5. Also, the helical phase in Eq. 2.9, is being replicated at the positions determined by the delta function (Eq. 2.6). Hence, we expect the vortex charge of the vortices in the array to acquire same order as of the input beam.

On the other hand, $J_{p,q}(m)$, the Bessel functions of first kind of orders p and q, as represented in Eq. 2.7, determines the overall intensity distribution of the vortex array (arrays of any

spatial profile) as a function of the phase contrast, m, of the MLA. Therefore, by changing the value of $m = 2\pi(n-1)s/\lambda$, with the change of any of the parameters, s and λ, one can control the overall intensity distribution of the vortex array. While the position of the individual vortex in the array is represented by the coordinates (p,q) with $(0,0)$ being the central vortex, their relative intensities are determined by the value of $J_{p,q}(m)^2$. Note that, here p and q are also the orders of Bessel functions of first kind. On the other hand, the pitch of the array given by $\Lambda_{exp} = \lambda d/\Lambda$, as shown in Eq. 2.6, is proportional to the distance of the MLA from the back focal plane of Fourier transform lens. Therefore, by simply adjusting, d, one can control the pitch of the vortex array.

To confirm the control in overall intensity pattern of the vortex array, we have used a MLA of lenslet thickness, $s = 1.31 \ \mu$m and pitch, $\Lambda = 300 \ \mu$m and numerically calculated the variation in the intensity pattern of vortex arrays for input wavelengths, $\lambda = 1064$ nm and $\lambda = 532$ nm, corresponding to the phase contrasts, $m = 1.11\pi$ and $m = 2.27\pi$ respectively. The results are shown in Fig. 2.2.

As evident from the first column, (a)-(b), of Fig. 2.2, we clearly see the change in the overall intensity pattern of the vortex array with the change in the phase contrast, m, of the MLA. Similarly, we have experimentally recorded the intensity pattern of the vortex array by using laser beams at 1064 nm and 532 nm as shown in second column, (c)-(d), of Fig. 2.2, in close agreement with the theoretical results. It is also interesting to note that, the decrease in the pitch, $\Lambda_{exp} = \lambda d/\Lambda$, of the vortex array with the decrease of the laser wavelength from 1064 nm to 532 nm, increases the total number of vortices in the array. In addition, the same intensity pattern can also be achieved by varying thickness, s, of the lenslets of MLA. Therefore, one can achieve vortex array beam of desired intensity pattern at a fixed wavelength by simply fabricating the lenslets of suitable thickness.
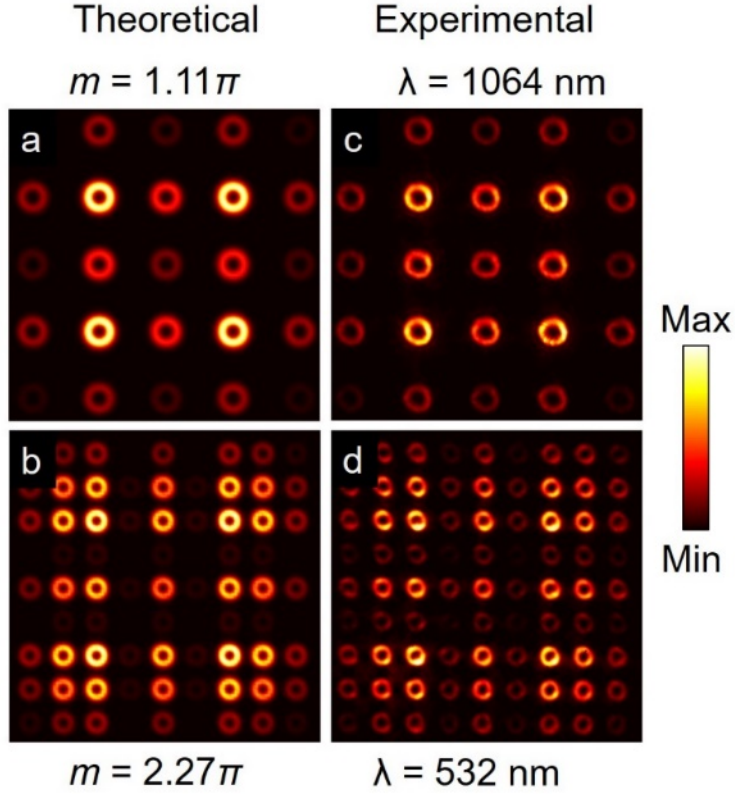
Figure 2.2: (a)-(b) Theoretical and corresponding (c)-(d) experimental intensity distributions of vortex arrays of order $l = 3$ for different values of phase contrast, m. Experimentally the phase contrast, m is varied using lasers of wavelength 1064 nm and 532 nm.

2.4   Results / Discussion

To verify the control in the pitch of the vortex array, we have Fourier transformed the input vortex beam of order $l = 1$ using the lens, L3, of focal length, $f = 300$ mm by keeping the MLA after the lens (Fig. 2.1). Keeping the CCD camera fixed at the Fourier plane, we have recorded the intensity distribution of the vortex array for different positions, d, of the MLA away from the camera. As evident from Fig. 2.3. (a)-(c), showing the intensity distribution of the vortex array for $d = 120$ mm, 160 mm and 240 mm respectively, the separation of the individual vortices is increasing with the increase of d without any change in the diameter of

the vortices. To get further insight, we have measured the pitch and the diameter of the vortices in the array for different values of d with the results shown in Fig. 2.3. (d). As evident from Fig. 2.3. (d), the pitch of the vortex array, Λ_{exp}, increases from 434 μm to 866 μm with the increase of MLA separation, d, from 120 mm to 240 mm. However, the diameter of the vortices remains constant around ~ 430 μm for all the positions of the MLA. While the upper limit of the pitch is decided by the focal length of the Fourier transforming lens, L3, the lower limit is decided by the mechical constraint to position the MLA close to the Fourier plane.
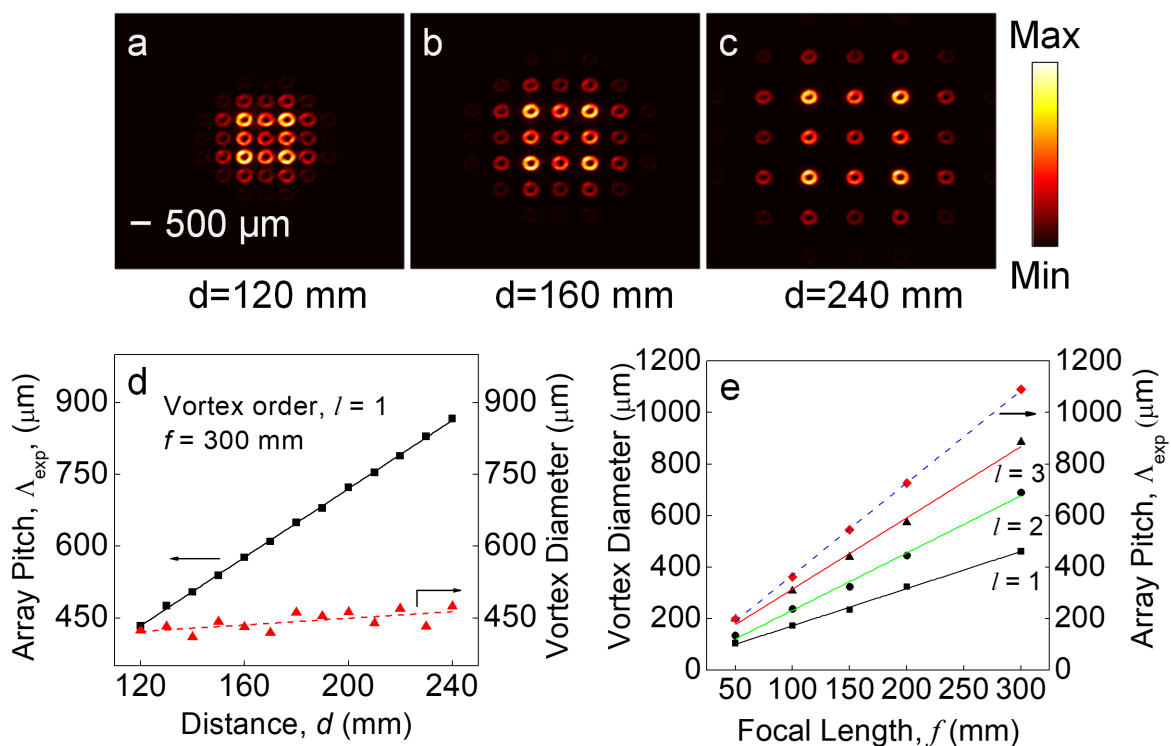
Figure 2.3: (a)-(c) Intensity distribution of the vortex array of order $l = 1$ for different position of the MLA. (d) Dependence of vortex beam diameter and pitch of the array on the distance d of MLA from the focal plane, (e) Variation of vortex beam diameter and pitch for input vortex orders, $l = 1$, 2 and 3 on the focal length of the Fourier transforming lens. Lines are linear fit to the experimental results.

23

Though the lower limit of the pitch is decided by the position of MLA close to the Fourier plane, the close packing of the beamlets in array, restricts further reduction in the pitch size. Fitting the experimental results with the theoretical expression of the vortex pitch, $\Lambda_{exp} = \lambda d/\Lambda$, (solid line), we have experimentally measured the pitch of the MLA to be, $\Lambda = 298\,\mu$m close to the standard value, $\Lambda = 300\,\mu$m as provided by the manufacturer. Such observation clearly confirms the current technique as a simple and straightforward way of measuring the pitch of the MLAs. We have also verified the control in the size of the vortices of orders, $l = 1, 2$ and 3 in the array by using a set of Fourier transforming lens, L3, of focal lengths, $f = 50, 100, 150,$ 200 and 300 mm. To avoid the mechanical constraint of keeping the MLA after the Fourier transforming lens especially for small focal lengths, we kept the MLA at a distance, f, before the lens and measured the size of the vortices at the Fourier plane. The results are shown in Fig. 2.3. (e). As evident from Fig. 2.3. (e), the diameter of the vortices of all orders, $l = 1, 2$ and 3, vary from 103 μm, 134 μm, and 198 μm to 460 μm, 690 μm, and 886 μm, linearly with the variation of focal length of the Fourier transforming lens from, $f = 50$ mm to $f = 300$ mm. As expected, for a fixed focal length of the Fourier transforming lens, the size of the vortices in the array increases with the order, l, of the input vortices. Similarly, the pitch of the vortex array of all orders as represented by, $\Lambda_{exp} = \lambda d/\Lambda$, varies linearly with the focal length of the Fourier transforming lens. As shown in Fig. 2.3. (e) (dashed line), the pitch varies linearly from 199 μm to 1091 μm with the focal length varying from $f = 50$ mm to $f = 300$ mm, independent to the order of the input vortex beam. Also, the experimentally measured value of MLA pitch from the best fit is observed to be, $\Lambda = 297\,\mu$m close to the standard value, $\Lambda = 300$ μm, provided by the manufacturer, thus confirming the potential of the current technique. It is also interesting to note that, for a fixed focal length, the pitch of the array, $\Lambda_{exp} = \lambda d/\Lambda$, is independent of the focal length. Hence one can achieve wide range of pitch values by using a single lens of longer focal length. All the experimental techniques discussed above to control the intensity distribution, size of the vortices in the array and the pitch of the array are equally applicable for beams of any input spatial profile.

With successful generation and control of the vortex arrays of different orders, we have also studied their frequency-doubling characteristics. Using the pump vortex array generated from the input vortex orders, $l_p = 2$ and 6, at 1064 nm with constant power of P = 3.5 W, we have frequency-doubled the arrays into green at 532 nm by placing the BiBO crystal at the Fourier plane. To avoid the mechanical constraint, the exit plane is imaged by using the lenses, L4 and L5 in a $4f$ ($f = 150$ mm) imaging configuration and recorded using CCD (Fig. 2.1). The results are shown in Fig. 2.4. Here we have shown nine spots of the arrays for better clarity without compromising on the scientific content of the experimental results. As evident from the first column, (a, b), of Fig. 2.4, both the arrays have beams with doughnut shaped intensity distribution. Using the tilted lens technique[6], splitting the vortices into their characteristic lobes, $n_p = l_p + 1$, as shown in the second column (c, d), of Fig. 2.4, we confirm that the vortices of each array have same order and sign. The order of the vortex arrays is measured to be, $l_p = 2$ and 6, same as that of the input vortex. Similarly, the corresponding second harmonic (SH) beam have intensity pattern same as that of the pump vortex array with nine doughnut shaped beams as shown in third column, (e, f) of Fig. 2.4. The tilted lens technique confirms the order of the SH vortex array as shown in fourth column, (g, h), of Fig. 2.4, to be $l_{sh} = 2 \times l_p = 4$ and 12 respectively, twice the order of the pump vortices satisfying the OAM conservation in the SHG process.

We have also measured the focusing dependent SHG efficiencies of vortex arrays of different orders. Keeping the pump power fixed at P = 3.5 W, we have pumped the crystal with vortex array of orders, $l_p = 0$ (Gaussian beam), 1, 2, and 3, using a set of lenses of focal lengths, $f = 25, 50, 100, 150, 200$ and 300 mm and recorded the SHG power. The results are shown in Fig. ref 5(a). As evident from Fig. 2.5 (a), like optical array of Gaussian beams ($l_p = 0$), the vortex array of all orders follow similar focusing dependent SHG efficiency showing maximum SHG efficiency for the focusing lens of $f = 50$ mm. Since the pitch of the vortex array does not change with its order, the decrease in SHG efficiency with the order of the vortex array at a fixed focusing condition can be attributed to the increase in the size of the vortex beam in the

25
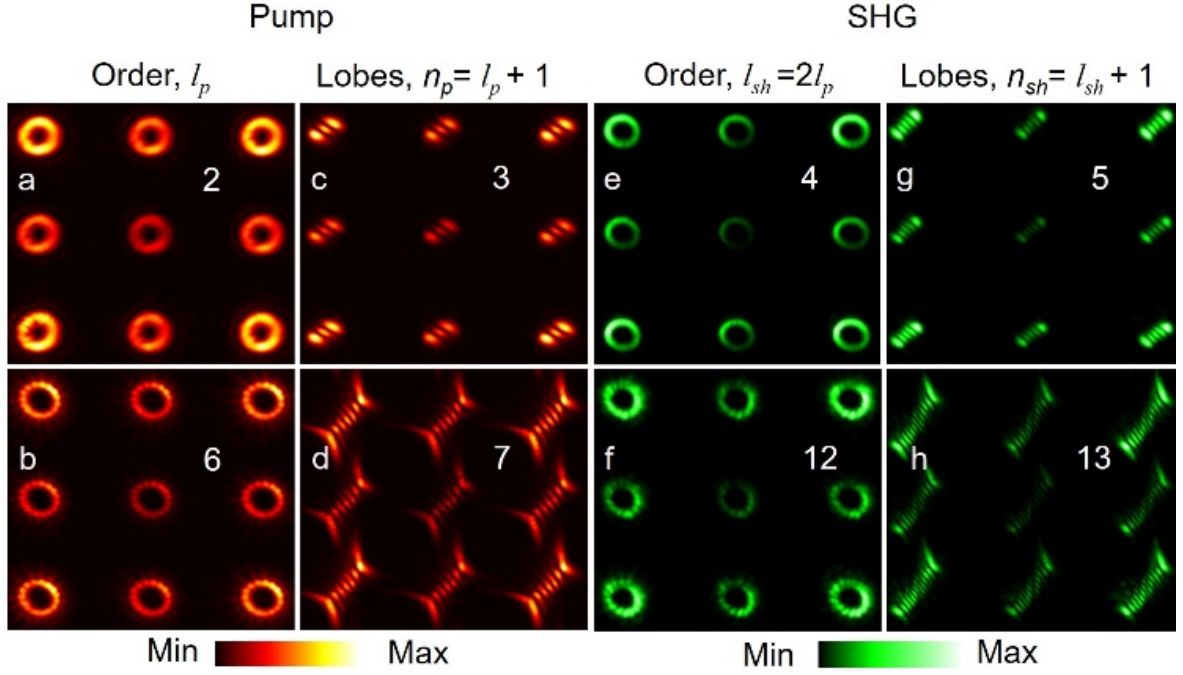
Figure 2.4: Intensity distribution of (a, b) vortex beams, and corresponding (c, d) lobe structure generated through the tilted lens of the pump vortex arrays of orders, $l_p = 2$ and $l_p = 6$. Corresponding (e, f) intensity distribution and (g, h) lobe structure of the SH vortex array.

array (see Fig. 2.3 (e)). Using the lens, $f = 50$ mm, the maximum single-pass SHG efficiency of the vortex array of orders, $l_p = 0$ (Gaussian beam), 1, 2, and 3, are measured to be 11.5 %, 3.6 %, 1.8 %, and 1.1 %, respectively. We have also measured the power scalability of the SH vortex array source. Focusing the vortex array of order, $l_p = 1$, using the lens of, $f = 50$ mm, we measured the single-pass SHG power and efficiency as a function of pump power with the results shown in Fig. 2.5 (b). As evident from Fig. 2.5 (b), the SHG power and efficiency of the vortex array show a quadratic and linear dependence, respectively, to the input pump vortex array power. The maximum SHG vortex array power is measured to be 138 mW at 3.8 W of pump power corresponding to a single-pass conversion efficiency as high as ~ 3.65 %. However, no saturation effect observed in the conversion efficiencies, indicating the possibility of increased SHG power with further increase in the pump power.
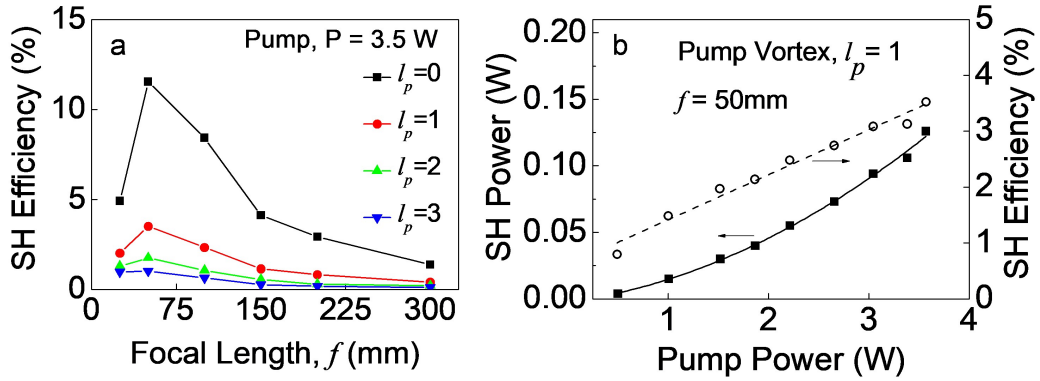
Figure 2.5: (a) Variation of SH efficiency of vortex arrays of different orders with the focal length of the focusing lens. Lines are guide to the eyes. (b) Dependence of SH vortex array power and efficiency on the power of the pump vortex array of order, $l_p = 1$. Solid and dotted linear are quadratic and linear fit to the experimental results.

2.5   Conclusions

In conclusion, we have demonstrated a generic experimental scheme based on a MLA and a Fourier transforming lens to generate high power, ultrafast, array beams with spatial intensity pattern same as the input beam. As a proof-of-principle, using input vortex beam of order as high as $l = 6$, we have generated vortex beam arrays. By placing the MLA after the Fourier transforming lens and subsequently adjusting the position of the MLA and focal length of the Fourier lens, we have controlled the size and pitch of the vortex beams in the array. Further, using single-pass SHG of the vortex array at 1064 nm we have generated vortex array at 532 nm with vortex order as high as 12. We also observe the vortex array beam to follow the focusing dependent SHG efficiency similar to the Gaussian beam. The maximum power of the SH vortex array beam is measured to be 138 mW of order, $l_p = 1$ at a single-pass SHG efficiency of $\sim 3.65\%$.

Chapter 3

Near field diffraction effects of MLA : Talbot effect

This chapter constitutes the following work.

1. *Near field diffraction effects of a microlens array and second harmonic Talbot effect with variable Talbot length*,

   B. S. Harshith and G. K. Samanta.

   [*Manuscript under preparation*]

3.1   Introduction

Microlens arrays (MLAs), a 2D array of close packed lenslets, are optical elements designed to split the wavefront into multiple beamlets of equal energies. MLAs have found a great deal of attention, for their wide range of applications in wavefront sensing [27], material lithography [28] and also as tool for fundamental studies in supercontinuum generation [29]. Having a series of periodic lenslets, they are also being used as array illuminators, and in ultrafast laser filamentation experiments. In 1836, a British scientist named Henry Fox Talbot, observed a unique self imaging effect while working on periodic gratings. When a plane wave is incident on a periodic grating, the image of the grating with the input field is replicated at a fixed lengths in the propagation direction, known as the Talbot lengths. The distance at the which the self

images are observed is known as the Talbot distance, z_T, given by $z_T = 2a^2/\lambda$. Here a is the period of the input grating object and λ is the wavelength of the input plane wave. The Talbot effect, being a near-field diffraction effect, is observed as a consequence of diffraction of the input field from the gratings, and the subsequent interference between the diffracted fields.

On the other hand, microlens arrays being 2D periodic objects are also expected to observe self imaging effects. Efforts have been made, to understand the near-field effects of MLA, and verified that the MLAs also exhibit the Talbot effect with almost similar properties [30]. However, there are other parameters, which play a crucial role in understanding the self-imaging effect in MLA. For, instance, lenslets which are not closely packed, introduced additional phases, resulting into a quasi-Talbot effect [31]. Though the Talbot imaging with MLAs has been studied in the past, not many works have been performed on the second harmonic (SH) Talbot effect. Recently, the SH Talbot effect has been observed, in quasi-phase matched crystals [32], in which the poling periodicity is used as a input periodic structure. However, due to low non-linear efficiencies in the direction perpendicular to the poling period, not much data can be recorded, over longer propagation distances.

Here we report for the first time, a generic experimental scheme to understand the single-pass second harmonic Talbot effect. Using the MLA as an array illuminator on to a 1.2 mm BiBO crystal at 1064 nm, we have recorded the self images in green at 532 nm. With the help of a suitable theoretical framework, we have also demonstrated a simple experimental scheme, based on Fourier transformation technique, to control the Talbot lengths of the MLA, in both pump and the second harmonics, overcoming the stringent dependence of input grating parameters on the Talbot length.

3.2 Experimental Setup

The schematic of the experimental setup is shown in Fig. 3.1. A 5 W Yb-fiber laser with spectral linewidth of 15 nm centred at 1064 nm providing femtosecond pulses of width $\sim$260

fs at a repetition rate of 78 MHz is used as the pump laser. The input power to the setup is varied using a half-wave plate ($\lambda/2$) and polarizing beam splitter cube (PBS1). The input beam is expanded and collimated using a telescopic combination lenses, L1 and L2 of focal length, $f = 50$ mm and $f = 100$ mm, to generate a near plane wave.
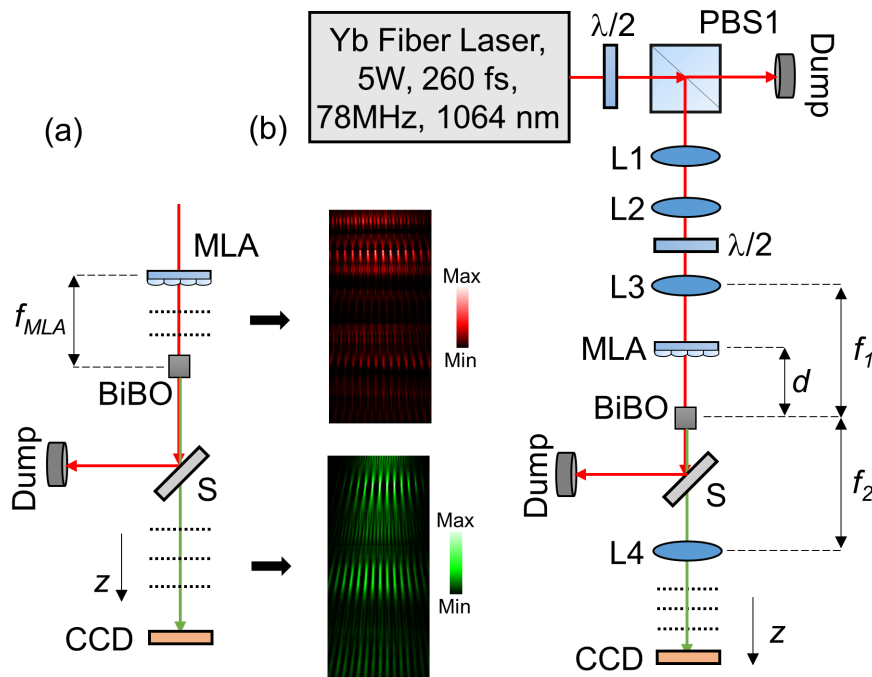
Figure 3.1: Schematic of the experimental setup to generate self-images of MLA, with (a) fixed and (b) variable Talbot lengths. $\lambda/2$, half-wave plate; PBS1, polarizing beam splitter cube; L1-4, plano-convex lenses; MLA, microlens array; BiBO, nonlinear crystal for frequency doubling; S, wavelength separator; CCD, CCD camera.

As shown in Fig. 3.1 (a), the plane wave on propagation through the microlens array (MLA) (Thorlabs MLA 300-14AR) consisting of 391 lenslets of focal length, $f_{MLA} = 18.6$ mm with a lenslet period of $\Lambda = 300\ \mu$m, generates self-images at 1064 nm in the Talbot planes. The CCD camera is scanned at a least count of 1 mm in the propagation direction, to obtain the transverse plane images. A 1.2 mm long and 4 x 8 mm^2 in aperture bismuth borate (BiBO) crystal, cut for type-I (e + e→o) frequency doubling in optical yz-plane ($\Phi = 90°$) with internal angle of $\theta=$

168.5° at normal incidence, is placed at the focal plane of the lenslets in the MLA, at a distance of f_{MLA} = 18.6 mm, for second harmonic generation (SHG) of the self-images at 1064 nm into green at 532 nm. The frequency-doubled images are extracted from the undepleted pump using a wavelength separator, S, and imaged to the CCD plane at multiple positions in the z-direction, at a least count of 1 mm. The insets in the Fig. 3.1 (a), show the line profiles of the self-images obtained in both pump and the SHG.

In order to overcome the stringent grating parameters on the Talbot lengths and to also obtain long range self images, it is essential to device a simple technique to control the Talbot lengths independently. Here we show another alternative experimental scheme to generate self-images at pre-decided positions, by changing the Talbot length of the MLA, without changing the MLA itself. The schematic of the experiment is shown in Fig. 3.1 (b). As noted, before, a plane wave generated by the combination of lenses, L1 and L2, is passed through a combination of plano-convex lens L3 of focal length, f_1 = 150 mm and the MLA. As suggested in our previous work [5], this generates an array of Gaussian beams, at the Fourier plane of lens L3. Now, an inverse Fourier transform is obtained by lens L4 of focal length f_2 = 150 mm, by positioning it at a distance, $f2$, from the Fourier plane of lens, L3. The CCD camera is scanned after the lens L4, to obtain the self-images. By controlling the distance, d, of the MLA, from the Fourier plane, the Talbot length of the self-images obtained can be precisely controlled. In the same experimental scheme (Fig. 3.1 (b)), by positioning the 1.2 mm long BiBO crystal at the Fourier plane of lens L3, we can control the Talbot length in second harmonic at 532 nm, with a much higher conversion efficiency. The wavelength separator, S, is used to filter out the undepleted pump.

3.3   Theory

As discussed before, when a plane wave is incident on a periodic grating, the self images are obtained at Talbot planes, in the direction of propagation. Considering the MLA of lenslet

period or the pitch, Λ, with a tightly packed lenslets, the Talbot length of an MLA can be given by,

$$z_T = 2\Lambda^2/\lambda \qquad (3.1)$$

Here, λ, is the input wavelength. A MLA can be approximated as a 2D sinusoidal phase grating [6]. Hence, contrary to an amplitude grating, where the self images are generated as a consequence of diffraction and interference, In the case of an MLA, the self images are evolved as a result of interference between the beamlets, after the focal plane. Therefore, the non-linear crystal is positioned at a distance of f_{MLA} from the MLA (Fig. 3.1 (a)). As the second harmonic generation process, generates photons at twice the wavelength of the input, it is expected that the Talbot length doubles in the SHG (Eq. 3.1, 3.2).

$$z_{T_{pump}} = \frac{2\Lambda^2}{\lambda_p} \qquad and \qquad z_{T_{shg}} = \frac{2\Lambda^2}{\lambda_{sh}} = \frac{4\Lambda^2}{\lambda_p} \qquad (3.2)$$

Here, λ_p and λ_{sh} are the wavelengths of the pump and second harmonic beams given by the relation, $\lambda_p = 2\lambda_{sh}$. As it can be seen, the pump and the SH, Talbot lengths are strictly dependent on the input parameters. In order to tune the Talbot length, we use the experimental scheme shown in Fig. 3.1 (b). The input electric field to the MLA, is Fourier transformed by lens L3 into an array of Gaussian beams at the focal plane of the lens L3 [6]. According to Fourier transformation theory [22], an object can be Fourier transformed by positioning the object (MLA) at a distance, $(f-d)$, after the lens. By using such a scheme of Fourier transformation, we can control the spatial transform at the Fourier plane, by changing the position, d, of the MLA, from the focal plane. As reported in Section 2.3, the pitch of the array, at the focal plane of lens L3, can be given by,

$$\frac{d}{f_1} \times \frac{f_1 \lambda_p}{\Lambda} = \frac{d\lambda_p}{\Lambda} = k\,(say), \qquad (3.3)$$

where, f_1, is the focal length of lens L3. For variable pump Talbot length, let us ignore the BiBO crystal at the Fourier plane of lens L3. The lens L4, of focal length, f_2, positioned at a distance f_2 from the Fourier plane of lens L3, obtains the inverse Fourier transform of the arrays. Hence, the effective lenslet period of the MLA, after the lens L4, can be obtained as,

$$\Lambda_{eff} = \frac{f_2 \lambda_p}{k} = \frac{f_2}{d} \Lambda. \tag{3.4}$$

By choosing the appropriate focal length of the lens L3 and L4, the effective lenslet period can be varied, which indeed results in variable Talbot length. The effective pump Talbot length can be given by,

$$z_T = \frac{2\Lambda_{eff}^2}{\lambda_p} = 2 \frac{f_2^2}{d^2} \frac{\Lambda^2}{\lambda_p} \tag{3.5}$$

For SH Talbot effect, the crystal is placed at the Fourier plane of lens L3. As similar to Eq. 3.4, in second harmonic generation process, the effective lenslet period of the MLA, after the lens L4, can be obtained as,

$$\Lambda_{eff} = \frac{f_2 \lambda_s}{k} = \frac{f_2 \lambda_s}{d \lambda_p} \Lambda = \frac{1}{2} \frac{f_2}{d} \Lambda. \tag{3.6}$$

It can be noticed that the effective lenslet period of MLA in SH is one-half to that of the pump. Consequently, the effective SH talbot length can be given by,

$$z_T = \frac{2\Lambda_{eff}^2}{\lambda_s} = \frac{1}{2} \frac{f_2^2}{d^2} \frac{\Lambda^2}{\lambda_s} = \frac{1}{2} \left[2 \frac{f_2^2}{d^2} \frac{\Lambda^2}{\lambda_p} \right]. \tag{3.7}$$

It can be observed that, the SH Talbot length is now one-half of the pump variable Talbot length,

which is in contrast to the experimental scheme (Fig. 3.1 (a)), where the SH Talbot length is twice that of the pump.

3.4   Results / Discussions

To verify the pump and the second harmonic Talbot effects, for the experimental scheme in Fig. 3.1 (a), we have recorded the transverse intensity distributions at a wavelength of $\lambda = 1064$ nm, with the help of a CCD camera. For the pump Talbot effect, we have recorded the images at 1 mm intervals, along the propagation direction. Due to mechanical constraint in positioning the CCD camera close to the MLA, we have recorded the data, starting from a point $\sim$5 cm from the MLA and upto a distance of 45 cm. However, this should not effect the scientific content of the experiment, as all the Talbot planes will get replicated at Talbot lengths, irrespective of their position of occurrence. For a better visibility in detecting the Talbot planes, we have plotted the line profiles of the CCD images, by extracting a fixed pixel line in every CCD image recorded, and concatenating all the pixel lines to form a continuous image. Fig. 3.2, shows the line profiles of the pump and SH beams. As it can be seen from Fig. 3.2 (a), the image positions identified with dashed lines are almost identical, indicating the position of a Talbot plane. It can be seen that, the intensity profile, indicated by the first dashed line and the third dashed line (Fig. 3.2 (a)), are almost identical, indicating the position of a full Talbot plane at a distance of Talbot length, $z_T = 171$ mm, close to the theoretically predicted value of $z_T = 169.1$ mm. It can be observed that, the half-Talbot plane ($\frac{z_T}{2}$), also has the same intensity profile as the Talbot plane, however, with careful observation, it can be noticed that the stripes observed in the half-Talbot plane are shifted by half a period in the vertical direction, as compared to the full Talbot planes. Similarly, for the case of SHG, we have recorded the CCD images at $\lambda = 532$ nm, immediately after the wavelength separator, S. Just from the initial comparisons between the pump and SHG line profiles in Fig. 3.2, it can be noticed that the Talbot length in

case of SHG is almost doubled. From the dashed lines, indicating the SHG Talbot planes, the Talbot length is estimated to around $z_T = 330$ mm, close to the theoretically predicted value of $z_T = 338$ mm. The decrease in the intensities with distance, can be attributed to the propagation losses in case of multiple beamlets. Also, the increase in divergence of SHG line profiles is due to the change in the beam-waists of the beamlets, after the SHG process.
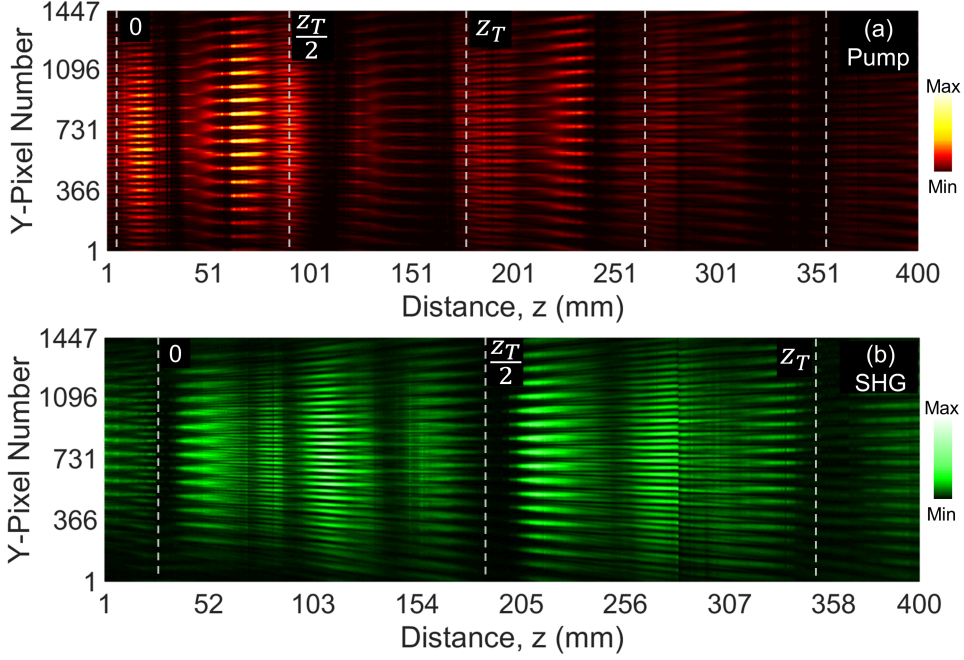
Figure 3.2: Line profiles of pump and SHG Talbot effects. (a) Pump Talbot effect, (b) SHG Talbot effect. (dashed lines are guides to Talbot planes)

To verify the control in the Talbot lengths in both pump and SHG, as suggested by the experimental scheme, Fig. 3.1 (b), we have positioned the MLA, at different distances, d, from the focal plane of lens L3 and recorded the change in longitudinal positions of pre-identified Talbot planes. Fig. 3.3, shows the intensity distributions of a specific Talbot plane, self imaged at different longitudinal positions, for two different positions of the MLA, $d = 125$ mm and $d = 150$ mm in both pump and SHG. For the current experiment, we used lenses L3 and L4 of focal lengths $f_1 = f_2 = 150$ mm, so that MLA can be positioned at multiple points. As

suggested from Fig. 3.3 (a)-(c), in case of pump Talbot effect, the same transverse image is observed at three longitudinal positions, indicating the Talbot length to be $z_T = 26$ cm for the MLA position, $d = 125$ mm. However, the same three intensity profiles are obtained at different longitudinal positions (Fig. 3.3 (d)-(e)), when the MLA is translated from $d = 125$ mm to $d = 100$ mm, with an increase in the Talbot length from $z_T = 26$ cm to $z_T = 40$ cm.
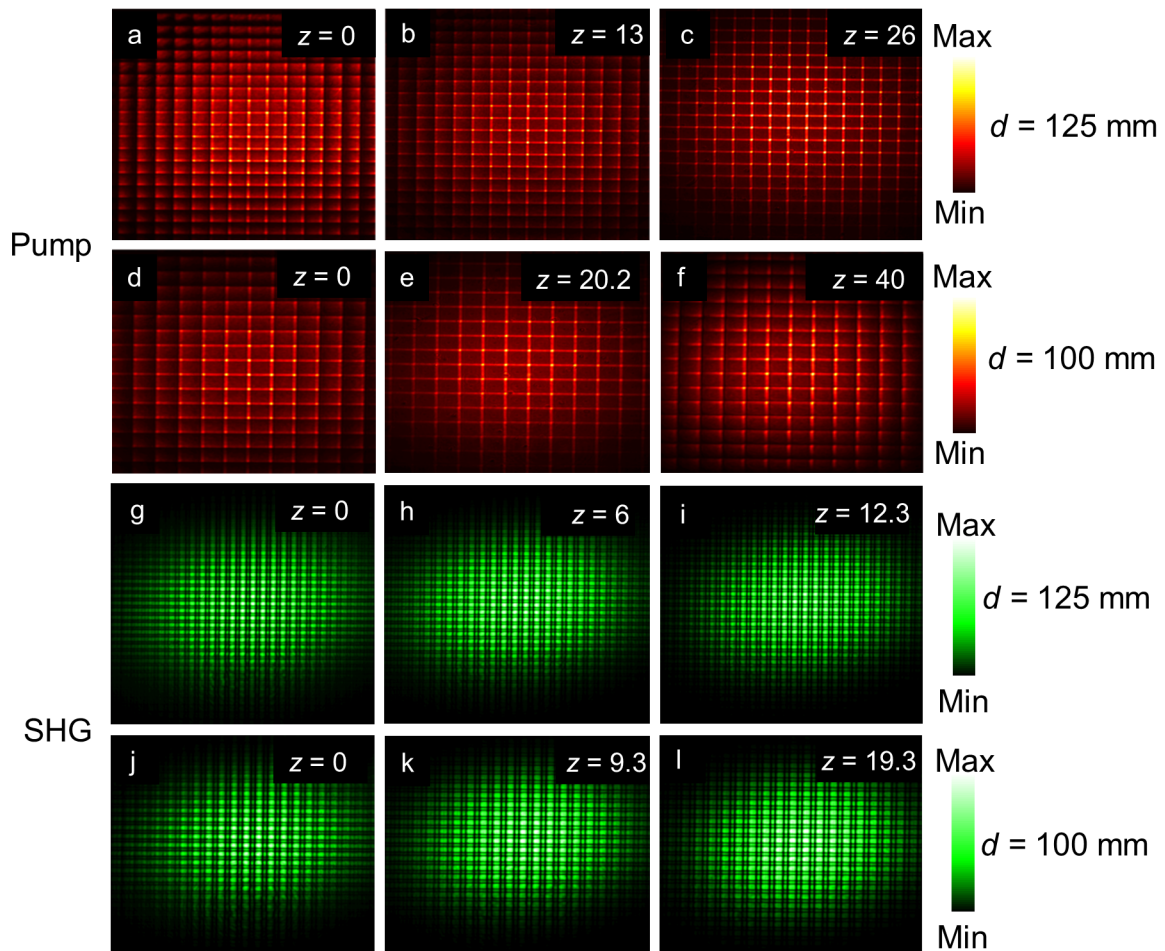

Figure 3.3: Intensity distributions of pump and SHG Talbot planes with MLA distance. (a) - (d) pump Talbot planes for MLA positions, $d = 125$ and 100 mm, (g) - (l) SHG Talbot planes for MLA positions, $d = 125$ and 100 mm.(z distances are in cm)

This observation is in accordance with Eq. 3.5, which suggests that, the closer the MLA is to

the focal plane of lens L3, the longer the Talbot length. Similarly, Fig. 3.3 (g)-(i), indicates the self-imaging of a particular SHG Talbot plane, obtained at three different longitudinal positions, with a Talbot length, $z_T = 12.3$ cm, for the MLA position, $d = 125$ mm. It can be noticed that, for the same MLA distance, the Talbot length in SHG is halved, contrary to the results of experimental scheme, Fig. 3.1 (a). As expected, the SHG Talbot length is also increased from $z_T = 12.3$ cm to $z_T = 19.3$ cm, with a change in MLA position from $d = 125$ mm to $d = 100$ mm. To get further insight, we have measured the Talbot lengths in both pump and SHG for different positions of the MLA, $d = 80$ mm, 90 mm, 100 mm, 110 mm, 120 mm and 125 mm, with results shown in Fig. 3.4.
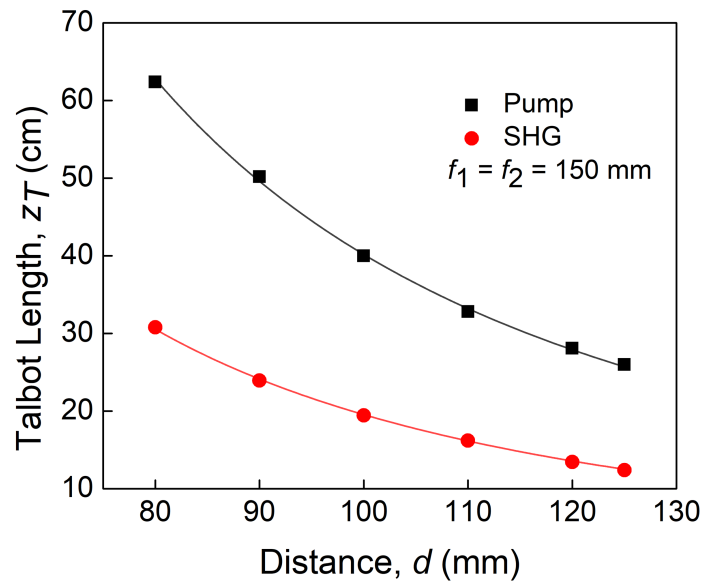
Figure 3.4: Dependence of pump and SHG Talbot lengths with the position of the MLA

As evident from Fig. 3.4, the pump Talbot length, z_T, decreases from 62.4 cm to 26 cm, with increase of MLA separation, d, from 80 mm to 125 mm. On the other hand, the SH Talbot length, decreases from 30.8 cm to 12.4 cm, for the same MLA separation. It can be seen that both the pump and SH Talbot lengths follow a inverse power law dependence, as suggested by the theoretical expressions, Eq. 3.5 and 3.7. Fitting the experimental results with the theoretical expressions (Eq. 3.5 and 3.7), we have experimentally measured the pitch of the MLA to be,

$\Lambda = 308.18\ \mu$m (pump fit) and $\Lambda = 303.98\ \mu$m (SHG fit), close to the standard value, $\Lambda = 300$ μm, provided by the manufacturer. Such an observation clearly confirms the current technique to control the Talbot lengths.

3.5   Conclusions

In conclusion, we have demonstrated the single pass second harmonic generation of Talbot effect using a microlens array (MLA). By illuminating the 1.2 mm long BiBO crystal with an MLA as an array illuminator, we have verified the doubling of the Talbot length in SHG. Also, using a novel experimental scheme based on Fourier transformation technique, we have shown a simple control to vary the Talbot lengths in both pump and SHG, without changing the MLA itself, thus overcoming the stringent dependence of input parameters on the Talbot lengths. With the help of current technique, we were able to tune the pump Talbot lengths from $z_T = 26$ cm to $z_T = 62.4$ and SHG Talbot lengths from $z_T = 12.4$ cm to $z_T = 30.8$ cm respectively. This generic experimental scheme can be used to generate long range self-images of periodic structures.

Chapter 4

Conclusion and scope for future work

4.1   Conclusion

In this Master's thesis, we have presented the study of,

(a) Generation and frequency conversion of array beams carrying orbital angular momentum,

(b) Near field diffraction effects of MLA and second harmonic Talbot effect.

In Chapter 1, we have covered the key concepts of structured optical beams and non-linear optics, which are extensively used throughout my Master's thesis work. It covers, structured optical beams, with an emphasis on vortex beams. We have also discussed the phase matching conditions in non-linear crystals and methods to achieve them. Finally, we have given the motivation and objective of the thesis work, along with brief content of each chapter.

In Chapter 2, we have demonstrated a simple and compact experimental scheme to generate high power, ultrafast, higher order vortex array beams. Using a dielectric microlens array (MLA) and a plano-convex lens, we have generated array beams carrying the spatial property of the input beam. Considering the MLA as a 2D sinusoidal phase grating, we have theoretically derived the parameters controlling the intensity pattern, size and the pitch of the array and verified experimentally. Using such array beams carrying OAM at 1064 nm, we have studied the non-linear interactions in second harmonic generation (SHG) process inside a 1.2 mm long

BiBO crystal and observed that the green vortex arrays at 532 nm, have orders, twice that of the pump arrays. Using lenses of different focal lengths, we have observed the vortex array of all orders to follow the focusing dependent non-linear conversion similar to that of a Gaussian beam. The maximum power of the green vortex array is measured to be 138 mW at a single-pass efficiency as high as ∼3.65%. This generic experimental scheme can be used to generate array beams of desired spatial profile across wide wavelength range by simply changing the spatial profile of the input beam.

In Chapter 3, we have demonstrated the single-pass second harmonic Talbot effect. By using the MLA as an array illuminator on to a 1.2 mm long BiBO crystal at 1064 nm, we have generated self images in green at 532 nm. We have observed that Talbot length in a single-pass second harmonic generation is twice that of the pump Talbot length. Also, using a suitable theoretical framework, we have developed a technique to control the Talbot lengths of the MLA, in both pump and SHG, with out changing the MLA itself. By using the current technique, we were able to tune the pump Talbot lengths from $z_T = 26$ cm to $z_T = 62.4$ and SHG Talbot lengths from $z_T = 12.4$ cm to $z_T = 30.8$ cm respectively. This generic experimental scheme can be used to generate long range self-images.

4.2   Scope for future work

As we have suggested in chapter 2, the experimental scheme for the generation of array beams is generic and can be implemented for any spatial profile. By utilizing the current technique with high power lasers and also with other spatial profiles, we would like to extend our studies in generating higher harmonics of the beam and also in single shot material lithography. As a continuation to the work demonstrated in Chapter 3, we plan to extend the self-imaging studies at a single-photon level by employing Spontaneous Parametric Down Conversion (SPDC) process.

References

[1] Oemrawsingh, S. S. R. et al. Production and characterization of spiral phase plates for optical wavelengths. *Applied optics*, **43**(3), 688-694 (2004).

[2] Marrucci, L., Manzo, C. and Paparo, D. Optical spin-to-orbital angular momentum conversion in inhomogeneous anisotropic media. *Phys. Rev. Lett.* **96**, 163905 (2006).

[3] Heckenberg, N. R., McDuff, R., Smith, C. P. and White, A. G. Generation of optical phase singularities by computer-generated holograms. *Opt. Letters* **17**, 221-223 (1992).

[4] Gbur, G. Singular Optics (*CRC Press*) (2017).

[5] Harshith, B.S. and Samanta, G.K. Controlled generation of array beams of higher order orbital angular momentum and study of their frequency doubling characteristics. *arXiv preprint*. arXiv:1903.00164 (2019).

[6] Vaity, P., Banerji, J. and Singh, R. P. Measuring the topological charge of an optical vortex by using a tilted convex lens. *Phys. Letters A* **377**, 1154-1156 (2013).

[7] Grier, D. G. A revolution in optical manipulation. *Nature* **424**, 810 (2003).

[8] Scott, T. F., Kowalski, B. A., Sullivan, A. C., Bowman, C. N. and McLeod, R. R. Two-color single-photon photoinitiation and photoinhibition for subdiffraction photolithography. *Science* **324**, 913-917 (2009).

[9] Wang, J. et al. Terabit free-space data transmission employing orbital angular momentum multiplexing. *Nat. Photon* **6**, 488 (2012).

[10] Mair, A., Vaziri, A., Weihs, G., and Zeilinger, A. Entanglement of the orbital angular momentum states of photons. *Nature* **412**, 313 (2001).

[11] Boyd, R.W. *Nonlinear optics.* Elsevier (2003).

[12] Apurv Chaitanya, N., Aadhi, A., Singh, R. P. and Samanta, G. K. Type-I frequency-doubling characteristics of high-power, ultrafast fiber laser in thick BIBO crystal. *Opt. Lett.* **39**, 5419-5422 (2014).

[13] Apurv Chaitanya, N., Aadhi, A., Jabir, M.V. and Samanta, G.K. High-power, high-repetition-rate, Yb-fiber laser based femtosecond source at 355 nm. *Opt. Lett.* **40**(18), pp.4269-4272 (2015).

[14] Apurv Chaitanya, N., Aadhi, A., Jabir, M. V. and Samanta, G. K. Frequency-doubling characteristics of high-power, ultrafast vortex beams. *Opt. Lett.* **40**, 2614-2617 (2015).

[15] Reicherter, M., Haist, T., Wagemann, E. U. and Tiziani, H. J. Optical particle trapping with computer-generated holograms written on a liquid-crystal display. *Opt. Lett.* **24**, 608-610 (1999).

[16] Omatsu, T. et al. Metal microneedle fabrication using twisted light with spin. *Opt. Express.* **18**, 17967-17973 (2010).

[17] Kumar, A., Vaity, P., Banerji, J., and Singh, R. P. Making an optical vortex and its copies using a single spatial light modulator. *Phys. Letters A,* **375**, 3634-3640 (2011).

[18] Liang, C. et. al. High-quality partially coherent Bessel beam array generation. *Opt. Lett.* **43**, 3188-3191 (2018).

[19] Sabatyan, A., and Fathi, B. High-efficiency arrays of any desired optical beams using modified grating-based elements. *Optical and Quantum Electronics.* **50**, 338 (2018).

[20] Gao, H. et. al. Quasi-Talbot effect of orbital angular momentum beams for generation of optical vortex arrays by multiplexing metasurface design. *Nanoscale.* **10**, 666-671 (2018).

[21] Knyazev, B. et. al. Quasi-Talbot effect with vortex beams and formation of vortex beamlet arrays. *Opt. Express.* **26**, 14174-14185 (2018).

[22] Goodman, J. W. Introduction to Fourier Optics. Roberts and Company Publishers. 81-83, 106-107 (2005).

[23] Alam, S. U., Rao, A. S., Ghosh, A., Vaity, P. and Samanta, G. K. Nonlinear frequency doubling characteristics of asymmetric vortices of tunable, broad orbital angular momentum spectrum. *Appl. Phys. Lett.* **112**, 171102 (2018).

[24] Teng, S., Zhang, N., Dong, Q. and Cheng, C. Diffraction of a one-dimensional phase grating in the deep Fresnel field. *JOSA A.* **24**(11), 3636-3643 (2007).

[25] George Barbastathis, Colin Sheppard, and Se Baek Oh. *2.71 Optics.* Massachusetts Institute of Technology: MIT OpenCourseWare, https://ocw.mit.edu, Spring (2009).

[26] Jabir, M. V., Chaitanya, N. A., Aadhi, A. and Samanta, G. K. Generation of '*perfect*' vortex of variable size and its effect in angular spectrum of the down-converted photons. *Sci. Reports* **6**, 21877 (2016).

[27] Liang, J., Grimm, B., Goelz, S. and Bille, J.F. Objective measurement of wave aberrations of the human eye with the use of a Hartmann-Shack wave-front sensor. *JOSA A.* **11**(7), pp.1949-1957 (1994).

[28] Aymerich, M., Nieto, D., ÃĄlvarez, E. and Flores-Arias, M. Laser surface microstructuring of biocompatible materials using a microlens array and the Talbot effect: evaluation of the cell adhesion. *Materials.* **10**(2), p.214 (2017).

[29] Camino, A., Hao, Z., Liu, X. and Lin, J. High spectral power femtosecond supercontin-uum source by use of microlens array. *Opt. lett.* **39**(4), pp.747-750 (2014).

[30] Besold, B. and Lindlein, N. Fractional Talbot effect for periodic microlens arrays. *Optical Engineering.* **36**(4), pp.1099-1106 (1997).

[31] Besold, B. and Lindlein, N. Practical limitations of Talbot imaging with microlens arrays. *Pure and Applied Optics: Journal of the European Optical Society Part A.* **6**(6), p.691 (1997).

[32] Zhang, Y., Wen, J., Zhu, S.N. and Xiao, M. Nonlinear talbot effect. *Phy. rev. lett.* **104**(18), p.183901 (2010).